J. Fluid Mech. (2022), *vol*. 953, A13, doi:10.1017/jfm.2022.929

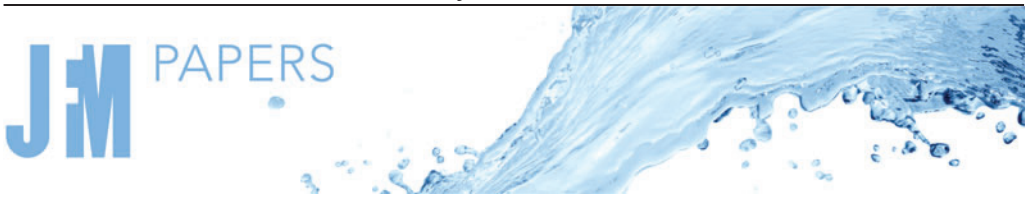

Electrohydrodynamic tuning of the migration characteristics of a sedimenting compound drop

Manash Protim Boruah[1], **Pitambar R. Randive**[1,†] **and Sukumar Pati**[1]

[1]Department of Mechanical Engineering, National Institute of Technology Silchar, Silchar-788010, India

(Received 11 April 2021; revised 13 October 2022; accepted 28 October 2022)

Electrohydrodynamic sedimentation of simple drops has been a topic well-studied by researchers. However, electrohydrodynamic sedimentation of a compound drop would be critically influenced by the density of the involved phases and this has hitherto remained unaddressed. Herein, we develop a semi-analytical model for an eccentric compound drop settling under the action of gravity and an electric field using bispherical coordinates. The sedimentation velocity of the two drops (shell and core) is determined, and the same is applied to capture the influence of concomitant physical, hydrodynamic and electric properties on compound droplet sedimentation. The findings indicate that the compound drop may either sediment or de-sediment depending on the amount of eccentricity and its interplay with electrohydrodynamic parameters. Thereafter, the critical limit of eccentricity and time within which similar results are furnished by concentric and eccentric configurations is determined. It is found that, based on the property ratios, the eccentricity remains lower than 0.1 up to a non-dimensional time range of the order of 10^2–10^3, within which both the configurations can furnish a similar solution.

Key words: drops, electrohydrodynamic effects

1. Introduction

Electrohydrodynamics has long been a topic of fascinating research interest owing to a wide variety of far-reaching industrial implications encompassing ink-jet printing (Basaran 2002), electrospraying (Jaworek & Krupa 1999; Castellanos 2014; Karyappa, Deshmukh & Thaokar 2014; Choi & Saveliev 2017; Gañán-Calvo *et al.* 2018), oil–water separation (Eow, Ghadiri & Sharif 2007), emulsification (Karyappa, Naik & Thaokar 2016) and so on. It all started with the benchmark finding of Taylor (1966), who applied a quasi-static electric field to a neutrally buoyant and leaky-dielectric liquid droplet under the conditions of weak deformation and negligible charge convection (CC). Taylor postulated a relation between the hydrodynamic and electrical property ratios that can predict whether the drop

† Email address for correspondence: pitambar@mech.nits.ac.in

© The Author(s), 2022. Published by Cambridge University Press

https://doi.org/10.1017/jfm.2022.929 Published online by Cambridge University Press

will become prolate or oblate when placed in an electrically conducive environment. This work of Taylor (1966) triggered many researchers (Ward & Homsy 2006; Lac & Homsy 2007; Zhang, Zahn & Lin 2013) to explore and address some of the neglected but yet effective facets of the study.

On this note, it is important to mention literatures that are not restricted to the assumptions of Taylor (1966), and instead observed the effects of an unsteady framework (Esmaeeli & Sharifi 2011) and the orientation of the applied electric field (Mandal, Bandopadhyay & Chakraborty 2016*a*; Poddar *et al.* 2019) on the electrohydrodynamic phenomenon; addressed the electrohydrodynamics of a droplet under an imposed background flow (Dey *et al.* 2015); considered the complicated influence of surface CC through a nonlinear coupling (Das & Saintillan 2016; Poddar *et al.* 2019) and dictated the two-way coupled influence between interfacial deformation and electrohydrodynamic characteristics of the droplet (Ha & Yang 2000; Xu & Homsy 2006; Vlahovska 2011; Yariv & Almog 2016). In addition to surface CC and interfacial deformation, the inclusion of gravity as a body force on the droplet would result in a coupled effect due to the imposition of an external electric field – a phenomenon that can non-trivially dictate the electrohydrodynamic sedimentation of drops. Indeed, such a mechanism is of immense importance (Bandopadhyay *et al.* 2016; Poddar *et al.* 2018) because of its applicability in processes such as drug transportation and enzyme crystallization (Zheng, Tice & Ismagilov 2004; Pethig 2013).

It is important to note that the above cited literatures are limited to studies on single droplet electrohydrodynamics. An advanced version of the same would include the analysis of a 'compound drop' (a core drop bounded by a shell drop) when it is affected by an electric field. Such works on compound drops are essential as they mimic the physical attributes associated with applications involving lipid bilayer formation (Palaniappan & Daripa 2000), recovery of oil (Stone & Leal 1990), phase separation (Draxler & Marr 1986) and drug transportation (Nakano 2000; Fabiilli *et al.* 2010). At the initial stage, investigations on compound drops were centred around studies like creeping flow mediated dynamics of a compound drop under the influence of buoyancy by Rushton & Davies (1983) and inertia by Brunn & Roden (1985); translational stability of compound drops by Sadhal & Oguz (1985); influence of extensional flows on the compound drop dynamics by Stone & Leal (1990) and many others of the kind extensively reviewed in Johnson & Sadhal (1985) – literatures that neglected the effect of an externally imposed electric field. However, an electric field, after it has been widely applied and proved effective in modulating the sedimentation of single drop (Xu & Homsy 2006; Bandopadhyay *et al.* 2016; Poddar *et al.* 2018), was applied to compound drops to understand the electrohydrodynamics involved.

The earliest literature investigating the stability of an eccentric compound drop due to the effect of buoyancy and an electric field was presented by Gouz & Sadhal (1989). They coupled the leaky-dielectric model to the creeping flow equations and semi-analytically solved the same for spherical drops in a bipolar coordinate system. Tsukada *et al.* (1997) conducted experiments and computations to gain insight into the concomitant effects of an electric field and convection on the degree of deformation of a compound drop. Finally, the authors showed that the electric intensity and the core to shell drop volume ratio could correlate the deformation of the drop and the strength of flow. For leaky-dielectric fluids, Behjatian & Esmaeeli (2013) analytically showed that the flow pattern inside and outside a compound drop subjected to a weak electric field is dictated by the number of vortices in the shell. Soni, Juvekar & Naik (2013) observed shape transition (oblate to prolate or

https://doi.org/10.1017/jfm.2022.929 Published online by Cambridge University Press

vice versa) for a double emulsion under a uniformly oriented electric field. Thereafter, the electrohydrodynamics of a compound drop was studied under an alternating current environment in some literature (Soni, Dixit & Juvekar 2017; Soni, Thaokar & Juvekar 2018).

Recently, Santra, Mandal & Chakraborty (2019) considered the pressure driven flow of a compound droplet in a transversely applied electric field. Their study addressed the droplet pinch-off dynamics because of a displacement of the core from the concentric point. The authors also examined the transient electrohydrodynamic phenomenon of a confined compound drop through numerical and analytical techniques in one of their works (Santra, Das & Chakraborty 2020). However, surface CC was not accounted for in any of the aforementioned literature. Moreover, the involved electrohydrodynamics can also be tuned by the deformation of the compound drop (Bandopadhyay *et al.* 2016). Hence, it has been established for simple drops that shape deformation and CC act as two key electrohydrodynamic determinants (Mandal *et al.* 2018). In the latest work from our group (Boruah *et al.* 2022), one such study was taken up where the problem of a compound drop moving under the action of background plane Poiseuille flow and acted upon by an applied electric field was investigated. In this case, a neutrally buoyant compound drop configuration is considered to highlight the sole effect of background flow. However, if the compound drop is allowed to sediment under the action of buoyancy in an electrically conducive environment, then the physics of the problem would be governed by a balance between the associated forces and the buoyancy force. In such a situation, the electrohydrodynamics of the compound drop would be critically influenced by the density of the involved phases, and this would be an interesting problem to investigate.

Motivated by the same, the buoyancy driven settling of a compound drop in an electrically conducive environment is analytically formalized for both the concentric and eccentric configurations. A detailed study is carried out for an eccentric compound drop subjected to applied electric field and is solved semi-analytically in a bispherical coordinate system in this article; however, a similar study for a concentric compound drop configuration can be performed using the method outlined in Boruah *et al.* (2022). For both the cases, the sedimentation velocity of the two drops (shell and core) is determined, and the same is applied to capture the influence of concomitant physical, hydrodynamic and electric properties on compound droplet sedimentation. Thereafter, the critical limit of eccentricity and time within which similar results are furnished by concentric and eccentric configurations is determined.

2. Problem formulation

2.1. *Physical description*

A physical scenario of an eccentric compound drop with R_o as the outer radius and R_i as the inner radius of the undeformed configuration that sediments with *a priori* unknown uniform shell drop velocity ($\boldsymbol{U}_2$) and core drop velocity ($\boldsymbol{U}_3$) in a surrounding unbounded phase due to the co-presence of gravity and an electric field ($\boldsymbol{E}_\infty$) uniformly applied, as shown in figure 1(*a*), is considered. A bispherical coordinate system (ξ, η, φ) is considered which is attached to the centroid of the drop. In the schematic, $\xi_1 = \cosh^{-1}((1 + e^2 - K^2)/2e)$ represents the shell drop interface and $\xi_2 = \cosh^{-1}((1 - e^2 - K^2)/2eK)$ denotes the core drop interface, where e indicates the eccentricity and K indicates radius ratio, i.e. the ratio of the radius of the core drop to the radius of the shell drop. Note that the numbers 1, 2 and 3 are used to designate the suspending phase, the shell drop phase and the core drop phase, respectively. Density is denoted by ρ_i, viscosity by μ_i, electrical permittivity

https://doi.org/10.1017/jfm.2022.929 Published online by Cambridge University Press

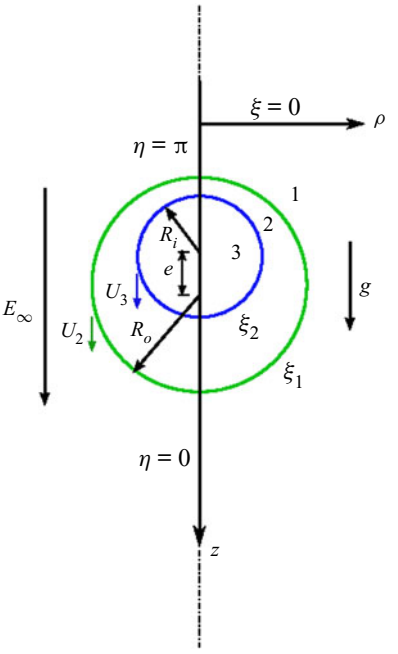

Figure 1. Representative schematic of an eccentric compound drop configuration sedimenting in the presence of both gravity and a uniform imposed electric field.

by ε_i and electrical conductivity by σ_i for the ith fluid. On the other hand, subscript 'ij' is used to refer to the interface separating the ith and jth fluids and, accordingly, we denote the interfacial tension by γ_{ij}.

2.2. *Assumptions*

The mathematical model is simplified using the following assumptions:

(i) The flows in all the three phases of fluids are considered to be incompressible. The core drop is not miscible in the shell and similarly the shell drop is immiscible in the suspending medium.
(ii) The fluids are considered to be leaky dielectric and Newtonian in nature.
(iii) Each of the fluid phases flows at a hydrodynamic Reynolds number ($Re = \rho_1 U_c R_o/\mu_1$) much less than unity such that the Stokes equations are applicable. Here, U_c is the characteristic velocity defined as $U_c = R_o^2 g\rho_1/\mu_1$, where g is defined as the acceleration due to gravity.
(iv) Under the creeping flow limit, the magnitude of the capillary number ($Ca = \mu_1 U_c/\gamma_{12}$) is considered to be low enough such that the spherical shape of the drops is maintained.
(v) At all times, quasi-steady flow is maintained such that the fluid motion is dictated by the instantaneous droplet position.
(vi) The stability of the compound drop system is maintained.

2.3. *Experimental justification for the assumptions*

The present theory has been set up on the assumptions outlined in the previous section and requires a suitable parametric space to connect itself to real world problems. To relate to practical experiments such as those in Xu & Homsy

https://doi.org/10.1017/jfm.2022.929 Published online by Cambridge University Press

(2006), we consider the suspending medium and the core drop to be castor oil ($\rho_{1,3} = 961$ kg m^{-3}, $\mu_{1,3} = 1.4$ Pa s, $\epsilon_{1,3} = 4.45\epsilon_0$, $\sigma_{1,3} = 5 \times 10^{-10}$ S m^{-1}), where ϵ_0 as the permittivity of vacuum, while phenylmethylsiloxane-dimethylsiloxane ($\rho_2 = 1000$ kg m^{-3}, $\mu_2 = 0.5$ Pa s, $\epsilon_2 = 2.8\epsilon_0$, $\sigma_2 = 10^{-12}$ S m^{-1}) is the shell drop fluid. The interfacial tension is taken to be $\gamma = 5 \times 10^{-3}$ N m^{-1}. To adhere to the assumptions considered herein, we consider $R_o = 200$ μm and $E_\infty = E_{ref} = 2 \times 10^5$ V m^{-1}.

With the aforementioned parametric set-up, the assumptions can be justified as follows: firstly, these fluids are Newtonian and immiscible, thus supporting assumptions (i) and (ii) in the previous section. They are also leaky dielectric (assumption (ii)) as the time scale for relaxation of charges, ε_1/σ_1 is less than the time scale for convection of charges, R_o/U_c. Stokes flow (assumption (iii)) is also valid as $Re \sim 10^{-4}$. The capillary number ($Ca \sim 0.1$) is low enough, thus validating assumption (iv). Although the compound drop would temporally evolve, the associated fluid motion would depend on the instantaneous location of the droplets, allowing us to consider quasi-steady flow (assumption (v)), as previously done in the literature (Pak, Feng & Stone 2014). Moreover, the generation of a stable compound drop (assumption (vi)) is practically feasible by actuating bi-phase flow in narrow capillaries (Utada *et al.* 2005; Kim *et al.* 2011).

2.4. *Non-dimensional scheme*

The non-dimensional scheme employs R_o as the length scale; $U_c = R_o^2 g\rho_1/\mu_1$ as the velocity scale; E_{ref} as the electric intensity scale; $\mu_1 U_c/R_o (= \boldsymbol{\tau}^H_{ref})$ as the hydrodynamic stress scale; and $\varepsilon_1 E^2_{ref} (= \boldsymbol{\tau}^E_{ref})$ as the electric stress scale. Similarly, we define different property ratios such as the viscosity ratio by $\lambda_{1i} = \mu_i/\mu_1$, conductivity ratio by $R_{1i} = \sigma_i/\sigma_1$, permittivity ratio by $S_{1i} = \varepsilon_i/\varepsilon_1$ and radius ratio by $K = R_i/R_o$.

2.5. *Governing equations and boundary conditions*

We start with the governing equation for electric field intensity i.e.

$$\boldsymbol{\nabla} \times \boldsymbol{E}_i = 0, \tag{2.1}$$

which can be reformulated as (Sadhal 1983)

$$\boldsymbol{E}_i = -\boldsymbol{\nabla}\psi_i = \boldsymbol{\nabla} \times \left(\frac{\omega_i}{\rho}\hat{\boldsymbol{\imath}}_\varphi\right). \tag{2.2}$$

Substituting (2.2) into (2.1) yields

$$\boldsymbol{\nabla} \times \boldsymbol{\nabla} \times \left(\frac{\omega_i}{\rho}\right)\hat{\boldsymbol{\imath}}_\varphi = 0, \tag{2.3}$$

where $\boldsymbol{\nabla} = \widehat{\boldsymbol{\imath}_\eta} h_1 \partial/\partial\eta + \widehat{\boldsymbol{\imath}_\xi} h_2 \partial/\partial\xi + \widehat{\boldsymbol{\imath}_\varphi} h_3 \partial/\partial\varphi$, $h_1 = h_2 = (\cosh\xi - \zeta)/c$ and $h_3 = (\cosh\xi - \zeta)/(c\sqrt{1-\zeta^2})$, with $\zeta = \cos\eta$ and $c = K\sinh\xi_1$.

Further simplification of (2.3) yields $\varepsilon^2\omega_i = 0$, with the expression for ε^2 as (Stimson & Jeffery 1926)

$$\varepsilon^2 \equiv \frac{(\cosh\xi - \zeta)}{c^2}\left[\frac{\partial}{\partial\xi}\left\{(\cosh\xi - \zeta)\frac{\partial}{\partial\xi}\right\} + (1-\zeta^2)\frac{\partial}{\partial\zeta}\left\{(\cosh\xi - \zeta)\frac{\partial}{\partial\zeta}\right\}\right]. \tag{2.4}$$

https://doi.org/10.1017/jfm.2022.929 Published online by Cambridge University Press

As given in Wacholder & Weihs (1972), ω has the following solution:

$$\omega = (\cosh\xi - \zeta)^{-1/2} \sum_{n=0}^{\infty} \left[d_n \cosh\left(n+\frac{1}{2}\right)\xi + e_n \sinh\left(n+\frac{1}{2}\right)\xi \right] C_{n+1}^{-1/2}(\zeta), \quad (2.5)$$

where, the Gegenbauer polynomial $C_{n+1}^{-1/2}$ is of degree $-1/2$ and order $(n+1)$. For different involved regions, ω_i has the following forms that satisfy the far field condition at the leading order ($\omega_1 \to \rho^2/2$, as $\xi, \eta \to 0$) and the boundedness condition ($|\omega_3| < \infty$, as $\xi \to \infty$) in bispherical coordinates (Morton, Subramanian & Balasubramaniam 1990)

$$\omega_1 = \frac{\rho^2}{2} + (\cosh\xi - \zeta)^{-1/2} \sum_{n=0}^{\infty} \left[d_n \sinh\left(n+\frac{1}{2}\right)\xi \right] C_{n+1}^{-1/2}(\zeta), \quad (2.6a)$$

$$\omega_2 = (\cosh\xi - \zeta)^{-1/2} \sum_{n=0}^{\infty} [f_n \, \mathrm{e}^{(n+1/2)(\xi-\xi_2)} + g_n \, \mathrm{e}^{-(n+1/2)(\xi-\xi_2)}] C_{n+1}^{-1/2}(\zeta), \quad (2.6b)$$

$$\omega_3 = (\cosh\xi - \zeta)^{-1/2} \sum_{n=0}^{\infty} [h_n \, \mathrm{e}^{\mp(n+1/2)(\xi-\xi_2)}] C_{n+1}^{-1/2}(\zeta). \quad (2.6c)$$

Utilizing the well-known relations $\rho = c\sqrt{1-\zeta^2}/(\cosh\xi - \zeta)$, $z = c\sinh\xi/(\cosh\xi - \zeta)$, $\varphi = \varphi$, the remaining boundary conditions will take the following form Gouz & Sadhal (1989):

$$\left.\frac{\partial \omega_i}{\partial \xi}\right|_{\xi=\xi_i} = \left.\frac{\partial \omega_j}{\partial \xi}\right|_{\xi=\xi_i}, \quad (2.7a)$$

$$R_{1i}\omega_i|_{\xi=\xi_i} = R_{1j}\omega_j|_{\xi=\xi_i}. \quad (2.7b)$$

Towards solving the flow problem, the governing equation $\varepsilon^4 S_i = 0$, with S being the Stokes streamfunction is used (Happel & Brenner 2012) which has a general solution of the following form for ith fluid (Stimson & Jeffery 1926):

$$S_i = (\cosh\xi - \zeta)^{-3/2} \sum_{n=0}^{\infty} \Xi_n^{(i)}(\xi) C_{n+1}^{-1/2}(\zeta). \quad (2.8)$$

As given in Mandal, Ghosh & Chakraborty (2016*b*), $\Xi_n^{(i)}$ will assume the following forms:

$$\Xi_n^{(1)} = D_n \, \mathrm{e}^{(n-1/2)\xi} + E_n \, \mathrm{e}^{(n+3/2)\xi} + \tilde{f}_n \, \mathrm{e}^{\mp(n-1/2)\xi} + \tilde{g}_n \, \mathrm{e}^{\mp(n+3/2)\xi}, \quad (2.9a)$$

$$\Xi_n^{(2)} = H_n \, \mathrm{e}^{(n-1/2)\xi} + I_n \, \mathrm{e}^{(n+3/2)\xi} + J_n \, \mathrm{e}^{\mp(n-1/2)\xi} + K_n \, \mathrm{e}^{\mp(n+3/2)\xi}, \quad (2.9b)$$

$$\Xi_n^{(3)} = L_n \, \mathrm{e}^{\mp(n-1/2)\xi} + M_n \, \mathrm{e}^{\mp(n+3/2)\xi}. \quad (2.9c)$$

Using these relations, the leading-order far field condition can be recast as (Mandal *et al.* 2016*b*)

$$S_1 = (\cosh\xi - \zeta)^{-3/2} \sum_{n=0}^{\infty} (\tilde{f}_n \, \mathrm{e}^{\mp(n-1/2)\xi} + \tilde{g}_n \, \mathrm{e}^{\mp(n+3/2)\xi}) C_{n+1}^{-1/2}(\zeta) \text{ as } \xi \to 0. \quad (2.10)$$

Here, the constants $\tilde{f}_n$ and $\tilde{g}_n$ can be expressed as (Mandal *et al.* 2016*b*)

$$\tilde{f}_n = \frac{n(n+1)c^2}{\sqrt{2}(2n-1)} U_2 \quad \text{and} \quad \tilde{g}_n = -\frac{n(n+1)c^2}{\sqrt{2}(2n+3)} U_2. \quad (2.11a,b)$$

https://doi.org/10.1017/jfm.2022.929 Published online by Cambridge University Press

The leading-order hydrodynamic boundary conditions are as follows (Gouz & Sadhal 1989):

$$u_\xi^{(i)} = u_\xi^{(j)} = \delta_{i2}(\boldsymbol{U}_3 - \boldsymbol{U}_2)\cdot\hat{\boldsymbol{i}}_\xi, \tag{2.12a}$$

$$u_\eta^{(i)} = u_\eta^{(j)}, \tag{2.12b}$$

$$\lambda_i\tau_{\xi\eta}^{(i)} - \lambda_j\tau_{\xi\eta}^{(j)} = \frac{E_\eta^{(i)}}{4\pi}(S_{1j}E_\xi^{(j)} - S_{1i}E_\xi^{(i)}). \tag{2.12c}$$

The electrostatic and hydrodynamic equations are first linearized to suitable forms given in Appendix A and Appendix B. Thereafter, they are solved semi-analytically using the procedure outlined in Boruah *et al.* (2022) and Jadhav & Ghosh (2021*a*), which is not repeated herein for the sake of brevity. This results in unknown coefficients which are then utilized along with force balance conditions to determine the velocities. The force balance equations are (Sadhal & Oguz 1985)

$$\aleph_{21}U_2 + \aleph_{31}U_3 + \aleph_1 = \frac{2}{3\sqrt{2}c}[K^3\rho_{13} + (1-K^3)\rho_{12} - 1], \tag{2.13a}$$

$$\aleph_{22}U_2 + \aleph_{32}U_3 + \aleph_2 = \frac{2}{3\sqrt{2}c}[K^3(\rho_{13} - \rho_{12})], \tag{2.13b}$$

where $\aleph_{21} = \sum_{n=0}^{N}(\vartheta_2^{(1)} + \vartheta_2^{(2)})$, $\aleph_{31} = \sum_{n=0}^{N}(\vartheta_3^{(1)} + \vartheta_3^{(2)})$, $\aleph_1 = \sum_{n=0}^{N}(\vartheta_1^{(1)} + \vartheta_1^{(2)})$ and so on.

3. Results and Discussion

First, the results for the shell and core drop velocities using the eccentric configuration and concentric configuration are compared under the small eccentricity limit ($e = 0.001$). The details of the solution procedure regarding sedimentation of a concentric compound drop can be found in Boruah *et al.* (2022). Note that the problem discussed in Boruah *et al.* (2022) is for a neutrally buoyant compound drop migrating under the action of plane Poiseuille flow and an electric field. However, the aforementioned problem can be simplified to the case of a compound drop sedimenting under the action of gravity and an electric field by setting the coefficients of the velocity profile accordingly and modifying the force balance condition to include the effect of density.

We start with a comparative study of the results for shell and core drop velocities using the eccentric configuration and concentric configuration under the small eccentricity limit and for two different combinations of R_{12} and S_{12} (i.e. $R_{12} < S_{12}$ and $R_{12} > S_{12}$), as shown in figure 2. As a function of radius ratio, the variation in velocity for the two drops are showcased in figures 2(*a*) and 2(*b*) for a suitable choice of parameter ratios as provided in the figure caption. The plots clearly indicate perfect matching between the results of the eccentric compound drop obtained using bispherical coordinates and the analytical results of a concentric compound drop. Moreover, we notice that the core size hinders the movement of both drops, as they slow down with the increase in K. However, the effect of K in altering the velocity is more pronounced in the core drop as compared with the shell drop. Furthermore, it is important to notice that both drops migrate in the direction of gravity when they are concentric (or eccentricity is very low), irrespective of the choice of R_{12} and S_{12}.

We also present a comparative study of the results for shell and core drop velocities using the eccentric compound drop configuration in the small eccentricity limit ($e = 0.001$), and

https://doi.org/10.1017/jfm.2022.929 Published online by Cambridge University Press

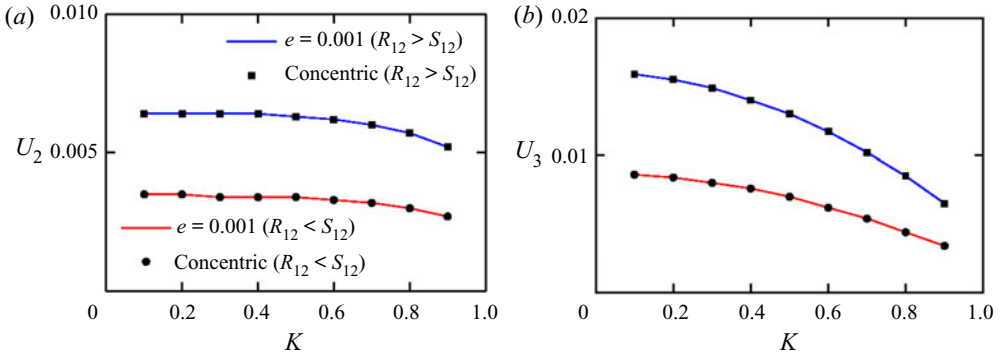

Figure 2. Comparison of (*a*) shell drop velocity (U_2) vs radius ratio (K) and (*b*) core drop velocity (U_3) vs K for eccentric compound drop with $e = 0.001$ and concentric compound drop for $R_{12} < S_{12}$ ($R_{12} = 1.5$, $S_{12} = 2$) and $R_{12} > S_{12}$ ($R_{12} = 1.1$, $S_{12} = 0.5$). The other considered ratios are $\rho_{12} = 1.04$, $\rho_{13} = 1$, $\lambda_{12} = 0.5$, $\lambda_{13} = 1$, $R_{13} = 1$ and $S_{13} = 1$.

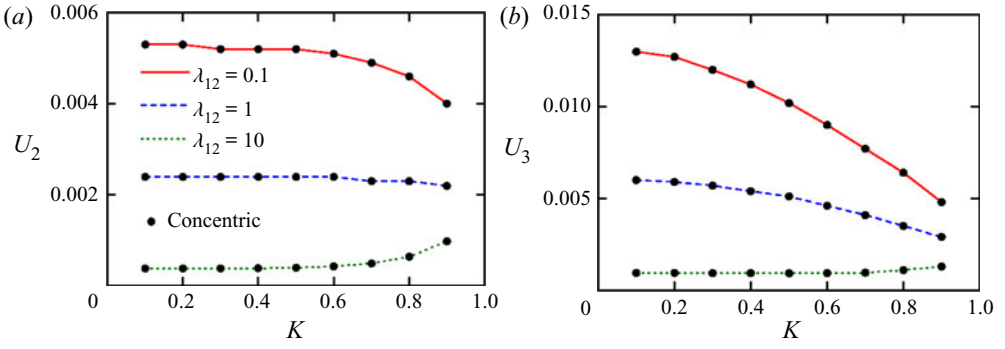

Figure 3. Comparison of (*a*) shell drop velocity (U_2) vs radius ratio (K) and (*b*) core drop velocity (U_3) vs K for eccentric compound drop with $e = 0.001$ and concentric compound drop for different values of λ_{12}. The other considered property ratios are $\rho_{12} = 1.04$, $\rho_{13} = 1$, $\lambda_{13} = 1$, $R_{12} = 1.5$, $R_{13} = 1$, $S_{12} = 2$ and $S_{13} = 1$.

for viscosity ratio values of 0.1, 1 and 10, and those of concentric compound drop in figure 3. As a function of K, the variation in velocity for the core and shell is, respectively, showcased in figures 3(*a*) and 3(*b*) for a suitable choice of parameter ratios, as mentioned in the caption of the figure. Here also, an accurate match between the results of the eccentric compound drop obtained using bispherical coordinates and the analytical results of the concentric case is noticed for different values of λ_{12}. The core and shell velocities decrease as λ_{12} increases. It is also important to notice that the size of the core drop can either aid or hinder the movement of the shell and core drop based on λ_{12}. Indeed for $\lambda_{12} \leq 1$, both the core and shell velocities decrease as K increases. On the contrary, for $\lambda_{12} > 1$, both the core and shell velocities increase with K owing to the decrease in volume of the highly viscous fluid in the shell drop.

Next, we move on towards analysing the impact of the hydrodynamic and electric parameters on the motion of an eccentric compound drop. We start with the variation of the core and shell velocities under the influence of the density ratio (ρ_{12}) for $e = 0.001$(concentric), 0.1, 0.3 and 0.5, as depicted in figure 4. The other relevant parameters are given in the caption of figure 4. We can notice the concomitant interplay

https://doi.org/10.1017/jfm.2022.929 Published online by Cambridge University Press

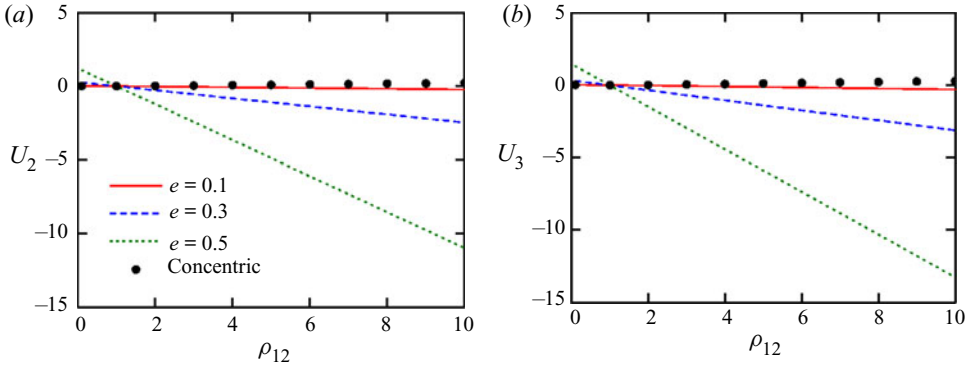

Figure 4. Variation of (*a*) shell drop velocity (U_2) and (*b*) core drop velocity (U_3) with ρ_{12} for $e = 0.1$, 0.3, 0.5 and 0.001 (concentric). The other considered parameters are $\rho_{13} = 1$, $\lambda_{12} = 0.5$, $\lambda_{13} = 1$, $R_{12} = 1.5$, $R_{13} = 1$, $S_{12} = 2$ and $S_{13} = 1$.

of eccentricity and density ratio in tuning the direction and speed of both drops. The velocities of the shell and core drop for $e = 0.1$ deviate minimally from the results for a concentric compound drop and show minimum alteration in the migration direction with change in ρ_{12}. However, with the increase in eccentricity, we observe that both drops migrate along the direction of the applied electric field when $\rho_{12} < 1$, while they migrate opposite to the direction of the applied electric field when $\rho_{12} > 1$. Also, the higher the deviation of the density ratio is from 1, the higher are the magnitudes of the core and shell velocities, and the same also increase as the eccentricity increases. The reason behind such an intriguing variation in the direction and velocity of core and shell because of the confluence of the eccentricity and density ratio can be attributed to the asymmetry in the fluid accumulated above and below the core with the change in eccentricity. Additionally, the presence of dense fluid either inside or outside the shell drop also aids or hinders the asymmetricity in the charge distribution due to the supplied electric field, thus mediating the droplet direction.

Figure 5 demonstrates the shell and core drop velocity variations as a function of viscosity ratio (λ_{12}) for $e = 0.001$(concentric), 0.1, 0.3 and 0.5, under a suitable choice of property ratios, as mentioned in the figure caption. At lower values of λ_{12}, the velocity variation is more significant as compared with that at higher values of λ_{12}. Indeed, a finite velocity occurs when the viscosity ratio is sufficiently higher. This underscores the profound influence of the presence of a viscous fluid either inside or outside the shell drop which aids or hinders the asymmetricity in the charge distribution because of the supplied electric field, thus manipulating the velocity of the drops. Apart from the effect of the viscosity in tuning the magnitude of the velocity, the eccentricity critically mitigates the direction of drop motion. For the concentric configuration and $e = 0.1$, the shell and core drops are seen to migrate along the direction of the applied electric field, while they migrate opposite to that of applied electric field when the eccentricity is sufficiently large. The asymmetry in the accumulated fluid above and below the core with a change in eccentricity is the reason behind such an observation.

In terms of the influence of the electric parameters, firstly, we show the variation of the shell and core drop velocities in figures 6(*a*) and 6(*b*), respectively, with a change in electrical conductivity ratio (R_{12}) for $e = 0.001$(concentric), 0.1, 0.3 and 0.5. The

https://doi.org/10.1017/jfm.2022.929 Published online by Cambridge University Press

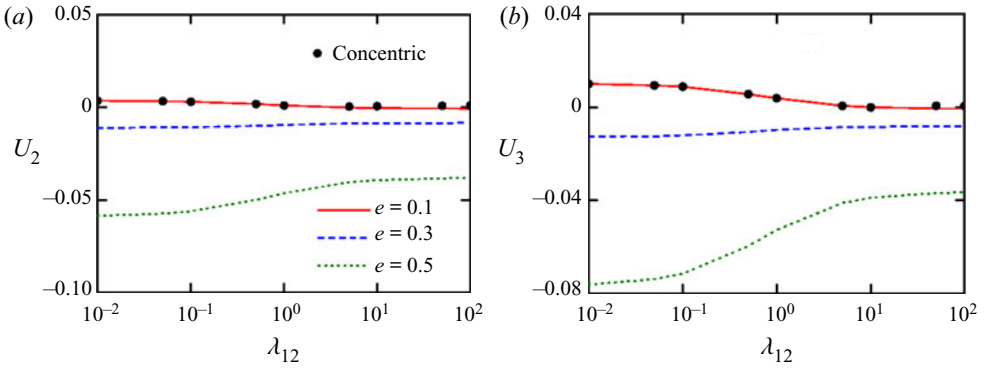

Figure 5. Variation of (*a*) shell drop velocity (U_2) and (*b*) core drop velocity (U_3) with λ_{12} for $e = 0.1, 0.3, 0.5$ and 0.001 (concentric). The other considered parameters are $\rho_{12} = 1.04$, $\rho_{13} = 1$, $\lambda_{13} = 1$, $R_{12} = 1.5$, $R_{13} = 1$, $S_{12} = 2$ and $S_{13} = 1$.

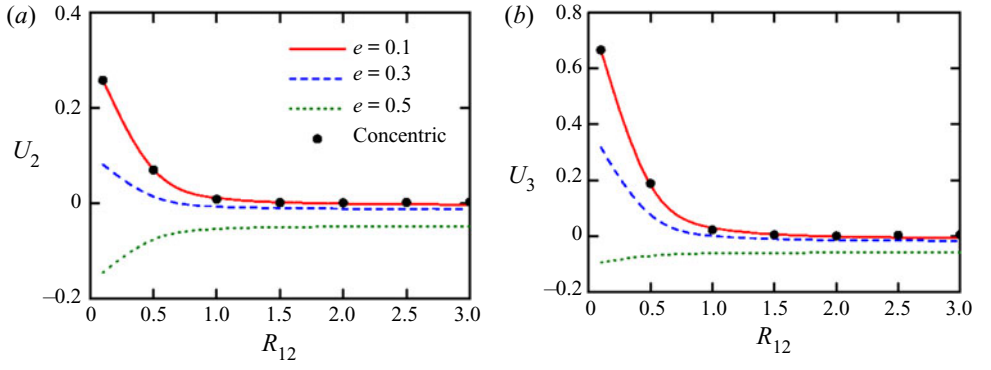

Figure 6. Variation of (*a*) shell drop velocity (U_2) and (*b*) core drop velocity (U_3) with R_{12} for $e = 0.1, 0.3, 0.5$ and 0.001 (concentric). The other considered parameters are $\rho_{12} = 1.04$, $\rho_{13} = 1$, $\lambda_{12} = 0.5$, $\lambda_{13} = 1$, $R_{13} = 1$, $S_{12} = 2$ and $S_{13} = 1$.

remaining property ratios considered here are given in the caption of figure 6. Here also, the variations in velocity with R_{12} for $e = 0.1$ and the concentric configuration depict close agreement. More precisely, we notice significant variation in the velocity when $R_{12} < 1$, beyond which the variation in velocity with R_{12} is insignificant. Quantitatively, the magnitudes of the core and shell velocities decrease as R_{12} increases and this decrease is sharp for $R_{12} < 1$. This happens because the asymmetricity in the charge distribution decreases with the increase in R_{12}. Also, it is to be noted that $S_{12} = 2$ in figure 6, and therefore, the core and shell velocities alter in sign when $R_{12} > 2$, depending also on the value of eccentricity. Indeed, when the eccentricity is sufficiently large, both the core and shell velocities remain negative (i.e. they migrate opposite to the direction of the applied electric field) throughout, irrespective of the variation in R_{12}. This happens because the imbalance in fluid accumulation above and below the core drop due to the variation of eccentricity nullifies the effect of the asymmetric charge distribution when the eccentricity is very large.

Figure 7 demonstrates the variation of shell and core drop velocities with electrical permittivity ratio (S_{12}) for $e = 0.001$(concentric), 0.1, 0.3 and 0.5. The remaining property ratios considered here are given in the caption of figure 7. As is evident, with the increase

https://doi.org/10.1017/jfm.2022.929 Published online by Cambridge University Press

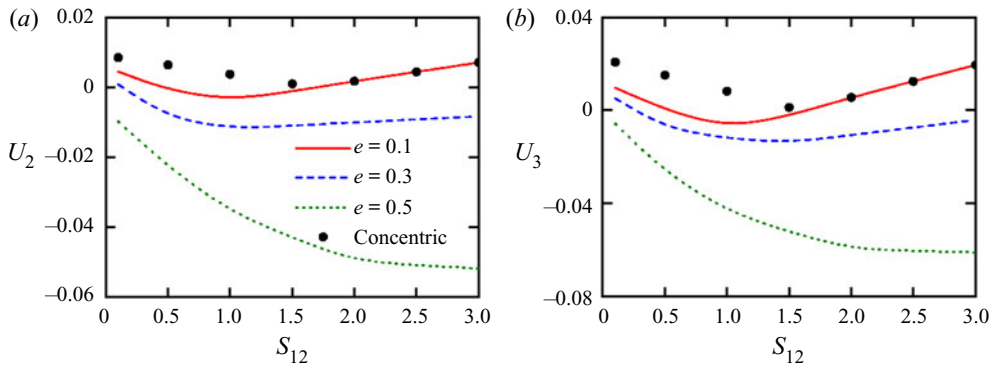

Figure 7. Variation of (*a*) shell drop velocity (U_2) and (*b*) core drop velocity (U_3) with S_{12} for $e = 0.1$, 0.3, 0.5 and 0.001 (concentric). The other considered parameters are $\rho_{12} = 1.04$, $\rho_{13} = 1$, $\lambda_{12} = 0.5$, $\lambda_{13} = 1$, $R_{12} = 1.5$, $R_{13} = 1$ and $S_{13} = 1$.

in S_{12}, the shell and core drop velocities may either decrease or increase or alter sign depending on e. More precisely, we notice an alteration in the migration direction of both the core and shell for $e = 0.1$, and an increase in the velocity of the drops when the eccentricity is sufficiently higher (i.e. $e = 0.5$) due to the increase in S_{12}. Such a variation occurs because the effect of the disbalance in fluid accumulation above and below the core due to the change in e nullifies the effect of the asymmetric charge distribution when the eccentricity is very large and, hence, we observe either an increase or decrease in velocity with the increase in S_{12}.

The next task is to explore whether an equilibrium configuration (for any e) exists and how the same is influenced by the hydrodynamic and electrical property ratios. We do so by plotting the variation of the relative velocity between the two drops (shell and core) i.e. U_2–U_3, for different values of eccentricity and observe its variation with a change in property ratios. Figure 8(*a*) shows the plot of U_2–U_3 variation as a function of ρ_{12}. At first, it is to be noted that, for $\rho_{12} < 1$, U_2–$U_3 < 0$, for almost all values of the eccentricity. This indicates faster movement of the core drop relative to the shell drop. However, when $\rho_{12} > 1$, U_2–$U_3 > 0$, for almost all values of the eccentricity. This alteration in sign indicates the presence of the critical density ratio ($\rho_{12} = 1$) for each e, for which $U_2 = U_3$. Also, the more the value of ρ_{12} is higher or lower than the critical ρ_{12}, the larger is the difference in the relative velocity of the two drops. Furthermore, we observe that the difference in the relative velocity is the lowest for the concentric configuration and $e \leq 0.1$, indicating the fact that the concentric compound drop furnishes similar results as the eccentric compound drop up to an eccentricity limit of 0.1, irrespective of the density ratio considered.

The existence of a non-zero relative velocity is indicative of the fact that the eccentricity of the compound drop evolves with time. With the progress of time, there is a linear increase in the rate of eccentricity (e) as follows: $e(t) = (U_{2,z}–U_{3,z})t$. Hence, for the validity of the concentric assumption, two conditions need to be satisfied. The first condition is that $e \ll 1$ or $|U_{2,z}–U_{3,z}| \ll 1$. Even though the first condition is satisfied, however, the eccentricity being a function of time would increase as time progresses. Therefore, $t < |U_{2,z}/(U_{2,z}–U_{3,z})|$ is the second essential condition for the validity of the concentric assumption. Indeed, our results quantitatively support the concentric compound drop assumption as shown in Appendix C.

This would continue until the core drop migrates, reaches a stable fixed point and moves with the same velocity as the shell drop thereafter. In order to ascertain the same, the

https://doi.org/10.1017/jfm.2022.929 Published online by Cambridge University Press

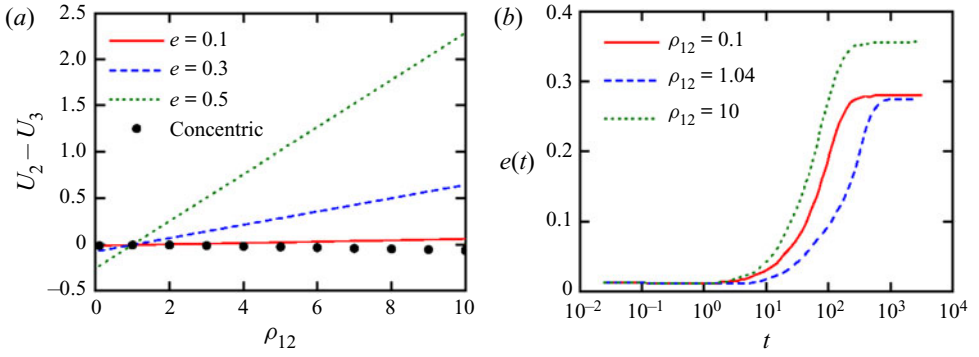

Figure 8. (*a*) Variation of (U_2–U_3) with ρ_{12} for $e = 0.1$, 0.3, 0.5 and 0.001 (concentric). (*b*) Evolution of eccentricity $e(t)$ with time (t), subjected to $e(t = 0) = 0$, for $\rho_{12} = 0.1$, 1.04 and 10. The other considered parameters are $\rho_{13} = 1$, $\lambda_{12} = 0.5$, $\lambda_{13} = 1$, $R_{12} = 1.5$, $R_{13} = 1$, $S_{12} = 2$ and $S_{13} = 1$.

following differential equation is solved numerically to determine how the eccentricity evolves with time:

$$\frac{\mathrm{d}e}{\mathrm{d}t} = [U_3(e(t), \Pi) - U_2(e(t), \Pi)]. \tag{3.1}$$

By solving (3.1), the temporal evolution of the eccentricity for different ρ_{12} is depicted in figure 8(*b*). From the figure, we observe that the closer the value of ρ_{12} is to the critical ρ_{12}, the smaller is the stable fixed eccentricity point and the larger is the time taken to attain the same. However, irrespective of the value of ρ_{12}, the eccentricity in general remains lower than 0.1 within a non-dimensional time limit of the order of 10^2. This indicates that the concentric compound drop configuration and eccentric configuration can furnish similar results until the time limit mentioned above.

In figure 9(*a*), we present the variation in the relative velocity of the core and shell with a viscosity ratio (λ_{12}) for different eccentricities. It clearly indicates that an equilibrium configuration exists at the critical viscosity ratio limit of around 10, deviation from which manifests as the core velocity being either higher or lower than the shell velocity. In fact, the least deviation from the stable equilibrium position is observed for an eccentricity near approximately 0.3. However, it is also seen that, irrespective of the value of λ_{12}, the concentric compound drop configuration predicts a similar variation in U_2–U_3 as that for $e = 0.1$. Moreover, to examine the point of stability in terms of eccentricity and non-dimensional time for different λ_{12}, we plot the temporal evolution of eccentricity for different λ_{12} in figure 9(*b*) by solving (3.1). From the figure, we observe that the closer the value of λ_{12} is to the critical viscosity ratio, the smaller is the stable fixed eccentricity point and the greater is the time taken to attain the same. However, irrespective of the value of λ_{12}, the eccentricity in general remains lower than 0.1 within a non-dimensional time range of the order of 10^2–10^3.

Next, we examine the implication of the electrical parameters for the relative drop velocity and for the temporal evolution of eccentricity. Figure 10(*a*) depicts the variation in the relative velocity of the core and shell with R_{12} for different eccentricities. The plot indicates maximum deviation from the stable equilibrium configuration for very small values of R_{12}. As R_{12} increases, the tendency of the core to attain a stable configuration increases, although it is the maximum when $R_{12} = S_{12}$. Moreover, the relative velocity of the drops increases with the decrease in eccentricity. We also observe that, irrespective of

https://doi.org/10.1017/jfm.2022.929 Published online by Cambridge University Press

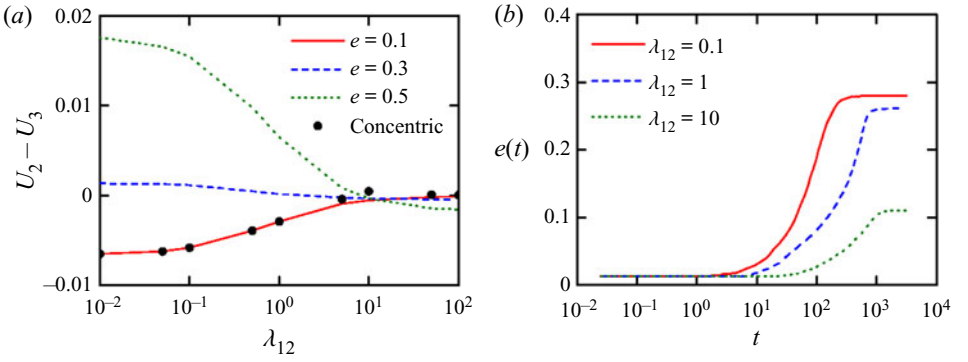

Figure 9. (*a*) Variation of $(U_2–U_3)$ with λ_{12} for $e = 0.1$, 0.3, 0.5 and 0.001 (concentric). (*b*) Evolution of eccentricity $e(t)$ with time (t), subjected to $e(t = 0) = 0$, for $\lambda_{12} = 0.1$, 1 and 10. The other considered parameters are $\rho_{12} = 1.04$, $\rho_{13} = 1$, $\lambda_{13} = 1$, $R_{12} = 1.5$, $R_{13} = 1$, $S_{12} = 2$ and $S_{13} = 1$.

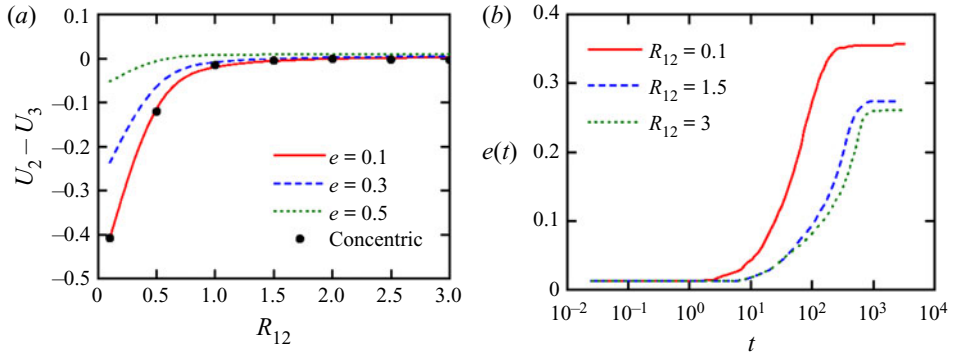

Figure 10. (*a*) Variation of $(U_2–U_3)$ with R_{12} for $e = 0.1$, 0.3, 0.5 and 0.001 (concentric). (*b*) Evolution of eccentricity $e(t)$ with time (t), subjected to $e(t = 0) = 0$, for $R_{12} = 0.1$, 1.5 and 3. The other considered parameters are $\rho_{12} = 1.04$, $\rho_{13} = 1$, $\lambda_{12} = 0.5$, $\lambda_{13} = 1$, $R_{13} = 1$, $S_{12} = 2$ and $S_{13} = 1$.

the value of R_{12}, the concentric compound drop configuration predicts a similar variation in $U_2–U_3$ as that for $e = 0.1$. Thereafter, to examine the point of stability in terms of eccentricity and non-dimensional time for different R_{12}, we plot the temporal evolution of eccentricity for different R_{12} in figure 10(*b*). From the figure, we observe that the smaller is deviation of R_{12} from the critical conductivity ratio, the smaller is the stable fixed eccentricity point and the larger is the time taken to attain the same. However, irrespective of the value of R_{12}, the eccentricity in general remains lower than 0.1 within a non-dimensional time limit of the order of 10^2, the condition under which the concentric and eccentric configurations furnish similar results.

Finally, the variation in the relative velocity of the core and shell with S_{12} for different eccentricities is presented in figure 11(*a*) for a suitable choice of property ratios, as mentioned in the figure caption. The plot indicates that $U_2–U_3$ is close to zero for $S_{12} = R_{12}$ when $e = 0.1$ for the concentric configuration, indicating $S_{12} = R_{12}$ as the critical permittivity limit pertaining to a stable configuration for this case. However, with the increase in eccentricity, we notice that the critical permittivity limit also changes. Thereafter, we plot the temporal evolution of the eccentricity for different S_{12} in figure 11(*b*) to examine the point of stability in terms of eccentricity and non-dimensional

https://doi.org/10.1017/jfm.2022.929 Published online by Cambridge University Press

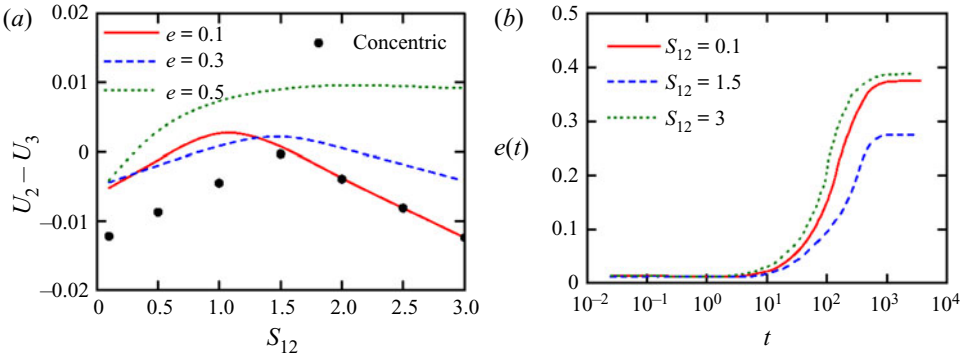

Figure 11. (*a*) Variation of $(U_2–U_3)$ with S_{12} for $e = 0.1$, 0.3, 0.5 and 0.001 (concentric). (*b*) Evolution of eccentricity $e(t)$ with time (t), subjected to $e(t = 0) = 0$, for $S_{12} = 0.1$, 1.5 and 3. The other considered parameters are $\rho_{12} = 1.04$, $\rho_{13} = 1$, $\lambda_{12} = 0.5$, $\lambda_{13} = 1$, $R_{12} = 1.5$, $R_{13} = 1$ and $S_{13} = 1$.

time for different S_{12}. We observe that smaller is the deviation of S_{12} from the critical permittivity ratio, the smaller is the stable fixed eccentricity point and the smaller is the time taken to attain the same. However, irrespective of the value of S_{12}, the eccentricity in general remains lower than 0.1 within a non-dimensional time limit of the order of 10^2. Under this condition, both configurations of compound drop furnish similar results.

4. Conclusions

Considering a practical situation of an eccentric compound drop sedimenting in the presence of a uniform electric field, we semi-analytically determine the sedimentation velocity of the two drops (shell and core), and the same is applied to capture the influence of concomitant physical, hydrodynamic and electric properties on compound droplet sedimentation. Thereafter, the critical limit of eccentricity and time within which similar results are furnished by the concentric and eccentric configurations is determined. The salient features of the present study for an eccentric compound drop can be summarized as follows:

(i) In the case of an eccentric compound drop, the density ratio critically controls the direction of migration of the drops when the eccentricity is high. However, the viscosity ratio tunes the magnitude of the shell and core drop velocities without affecting the direction of motion.

(ii) At lower values of the eccentricity, the core and shell alter their direction of motion when $R_{12} = S_{12}$, while they always migrate opposite to the direction of the applied electric field when the eccentricity is sufficiently large, irrespective of the variation in conductivity ratio. On the other hand, with the increase in S_{12}, the core and shell velocities may either decrease or increase or alter sign based on the eccentricity.

(iii) In terms of the relative velocity between the core and shell, there exists a critical hydrodynamic or electrical parameter ratio above or below which the core drop might move at a velocity higher or lower than the shell drop. This critical density ratio is 1 and the critical viscosity ratio is 10. In terms of the conductivity ratio, the critical ratio is at $R_{12} = S_{12}$. However, it is found that the critical permittivity limit also changes with eccentricity.

https://doi.org/10.1017/jfm.2022.929 Published online by Cambridge University Press

(iv) Moreover, regardless of the value of the parameter ratio, the concentric configuration can predict similar variation in the relative velocity as that obtained for $e = 0.1$ and hence, the concentric and eccentric compound drop configurations furnish similar results up to $e < 0.1$. Indeed, from the temporal evolution of the eccentricity, the stable fixed eccentricity point and the non-dimensional time required to attain the same are determined for different values of the property ratios. It is found that, based on the property ratios, the eccentricity remains lower than 0.1 up to a non-dimensional time range of the order of 10^2–10^3, within which both configurations can furnish similar solutions.

Acknowledgements. The authors would like to acknowledge U. Ghosh and S.N. Jadhav for insightful discussions regarding the numerical solution of eccentric compound drop configuration. The authors would also like to acknowledge S. Mandal for insightful discussions regarding the solution for the concentric compound drop configuration.

Declaration of interests. The authors report no conflict of interest.

Author ORCIDs.
Pitambar R. Randive https://orcid.org/0000-0002-7386-3902.

Appendix A. Algebraic equations for the electric potential field

The following linear algebraic equations are obtained by converting the boundary conditions (2.7) (Jadhav & Ghosh 2021*b*):

$$[-d_{n-1}R_{4n} + f_{n-1}R_{5n} - g_{n-1}R_{6n}](n+1) + d_n\Upsilon_{1n} - f_n\Upsilon_{2n} + g_n\Upsilon_{3n} + [-d_{n+1}R_{7n} + f_{n+1}R_{8n} - g_{n+1}R_{9n}]n = 4\sqrt{2}n(n+1)c^2\,\mathrm{e}^{\mp(n+1/2)\xi_1}\sinh\xi_1, \tag{A1a}$$

$$-[f_{n-1} - g_{n-1} + h_{n-1}](n+1) + f_n\Upsilon_{4n} - g_n\Upsilon_{5n} + h_n\Upsilon_{5n} - [f_{n+1} - g_{n+1} + h_{n+1}]n = 0, \tag{A1b}$$

$$-d_nR_{1n} + [f_nR_{2n} + g_nR_{3n}]R_{12} = 4\sqrt{2}n(n+1)c^2\,\mathrm{e}^{\mp(n+1/2)\xi_1}, \tag{A1c}$$

$$[f_n + g_n]R_{12} - h_nR_{13} = 0, \tag{A1d}$$

where, $R_{1n} = \sinh(n+1/2)\xi_1$; $R_{2n} = \mathrm{e}^{(n+1/2)(\xi_1-\xi_2)}$; $R_{3n} = \mathrm{e}^{-(n+1/2)(\xi_1-\xi_2)}$

$$R_{4n} = \cosh\left(n-\frac{1}{2}\right)\xi_1; \quad R_{5n} = \mathrm{e}^{(n-1/2)(\xi_1-\xi_2)}; \quad R_{6n} = \mathrm{e}^{-(n-1/2)(\xi_1-\xi_2)}; \tag{A2a–c}$$

$$R_{7n} = \cosh\left(n+\frac{3}{2}\right)\xi_1; \quad R_{8n} = \mathrm{e}^{(n+3/2)(\xi_1-\xi_2)}; \quad R_{9n} = \mathrm{e}^{-(n+3/2)(\xi_1-\xi_2)}; \tag{A3a–c}$$

$$\Upsilon_{1n} = (2n+1)\cosh\xi_1\cosh\left(n+\frac{1}{2}\right)\xi_1 - R_{1n}\sinh\xi_1; \tag{A4}$$

$$\Upsilon_{2n} = [(2n+1)\cosh\xi_1 - \sinh\xi_1]R_{2n}; \quad \Upsilon_{3n} = [(2n+1)\cosh\xi_1 + \sinh\xi_1]R_{3n}; \tag{A5a,b}$$

$$\Upsilon_{4n} = (2n+1)\cosh\xi_2 - \sinh\xi_2; \quad \Upsilon_{5n} = (2n+1)\cosh\xi_2 + \sinh\xi_2. \tag{A6a,b}$$

https://doi.org/10.1017/jfm.2022.929 Published online by Cambridge University Press

Appendix B. Algebraic equations for the hydrodynamic field

The algebraic equations for the hydrodynamic field are as follows:

$$D_n\Lambda_n^1 + E_n\Lambda_n^2 = U_2\Lambda_n^3\left(\frac{\Lambda_n^4}{(2n-1)} - \frac{\Lambda_n^5}{(2n+3)}\right), \tag{B1a}$$

$$H_n\Lambda_n^1 + I_n\Lambda_n^2 + J_n\Lambda_n^4 + K_n\Lambda_n^5 = 0, \tag{B1b}$$

$$(2n-1)\{(D_n - H_n)\Lambda_n^1 + J_n\Lambda_n^4\} + (2n+3)\{(E_n - I_n)\Lambda_n^2 + K_n\Lambda_n^5\} = -U_2\Lambda_n^3(\Lambda_n^4 - \Lambda_n^5), \tag{B1c}$$

$$\begin{aligned}&(2n-1)^2\{(D_n - \lambda_2 H_n)\Lambda_n^1 - \lambda_2 J_n\Lambda_n^4\} + (2n+3)^2\{(E_n - \lambda_2 I_n)\Lambda_n^2 - \lambda_2 K_n\Lambda_n^5\}\\ &\quad = \Lambda_n^6\left(\frac{S_{12}}{R_{12}} - 1\right)\left[\begin{array}{l}\dfrac{(2n+1)\Lambda_n^7}{2}\left\{c\Omega_{n,k}^1 - c^2\Omega_{n,k}^2 - \dfrac{1}{c}\Lambda_k^8\Omega_{n,k}^3 - \dfrac{1}{2c}\Lambda_k^9\Omega_{n,k}^4\right\}\\ \quad +\Lambda_n^{10}\sinh\xi_1\left\{-\dfrac{c}{2}\Omega_{n,k}^5 + \dfrac{c^2}{2}\Omega_{n,k}^6 + \dfrac{1}{2c}\Lambda_k^8\Omega_{n,k}^7 + \dfrac{1}{2c}\Lambda_k^9\Omega_{n,k}^8\right\}\end{array}\right]\\ &\quad - U_2\Lambda_n^3((2n-1)\Lambda_n^4 - (2n+3)\Lambda_n^5),\end{aligned} \tag{B1d}$$

$$H_n\Lambda_n^1 + I_n\Lambda_n^2 + J_n\Lambda_n^4 + K_n\Lambda_n^5 = (U_2 - U_3)\Lambda_n^3\left(\frac{\Lambda_n^4}{(2n-1)} - \frac{\Lambda_n^5}{(2n+3)}\right), \tag{B1e}$$

$$L_n\Lambda_n^4 + M_n\Lambda_n^5 = (U_2 + U_3)\Lambda_n^3\left(\frac{\Lambda_n^4}{(2n-1)} - \frac{\Lambda_n^5}{(2n+3)}\right), \tag{B1f}$$

$$(2n-1)\{H_n\Lambda_n^1 + (L_n - J_n)\Lambda_n^4\} + (2n+3)\{I_n\Lambda_n^2 + (M_n - K_n)\Lambda_n^5\} = 0, \tag{B1g}$$

$$\begin{aligned}&(2n-1)^2\{\lambda_2 H_n\Lambda_n^1 + (\lambda_2 J_n - \lambda_3 L_n)\Lambda_n^4\} + (2n+3)^2\{\lambda_2 I_n\Lambda_n^1 + (\lambda_2 K_n - \lambda_3 M_n)\Lambda_n^4\}\\ &\quad = \Lambda_n^6\left(\frac{S_{12}R_{13}}{R_{12}} - S_{13}\right)\left[\begin{array}{l}\dfrac{(2n+1)\Lambda_n^7}{2}\left\{-\dfrac{1}{c}\Lambda_k^8\Omega_{n,k}^3 - \dfrac{1}{2c}\Lambda_k^9\Omega_{n,k}^4\right\}\\ +\Lambda_n^{10}\sinh\xi_2\left\{\dfrac{1}{2c}\Lambda_k^8\Omega_{n,k}^7 + \dfrac{1}{2c}\Lambda_k^9\Omega_{n,k}^8\right\}\end{array}\right]\\ &\quad + (U_2 - U_3)(\lambda_2 - \lambda_3)\Lambda_n^3((2n-1)\Lambda_n^4 - (2n+3)\Lambda_n^5).\end{aligned} \tag{B1h}$$

The notations used in (B1) have the following expressions:

$$\begin{aligned}&\Lambda_n^1 = \mathrm{e}^{(n-1/2)\xi}, \quad \Lambda_n^2 = \mathrm{e}^{(n+3/2)\xi}, \quad \Lambda_n^3 = n(n+1)c^2/\sqrt{2},\\ &\Lambda_n^4 = \mathrm{e}^{-(n-1/2)\xi}, \quad \Lambda_n^5 = \mathrm{e}^{-(n+3/2)\xi},\end{aligned} \tag{B2a–e}$$

$$\Lambda_n^6 = \frac{n(n+1)(2n+1)}{2\pi}, \quad \Lambda_n^7 = f_n\,\mathrm{e}^{(n+1/2)(\xi-\xi_2)} - g_n\,\mathrm{e}^{-(n+1/2)(\xi-\xi_2)}, \tag{B3a,b}$$

$$\Lambda_k^8 = \sum_{k=0}^{N} d_k \sinh\left(k+\frac{1}{2}\right)\xi C_k^{1/2}, \quad \Lambda_k^9 = \sum_{k=0}^{N} d_k \sinh\left(k+\frac{1}{2}\right)\xi C_{k+1}^{-1/2}, \tag{B4a,b}$$

$$\Lambda_n^{10} = f_n\,\mathrm{e}^{(n+1/2)(\xi-\xi_2)} + g_n\,\mathrm{e}^{-(n+1/2)(\xi-\xi_2)}, \tag{B5}$$

https://doi.org/10.1017/jfm.2022.929 Published online by Cambridge University Press

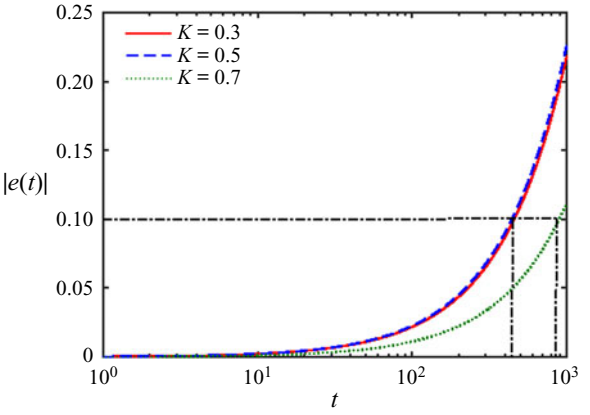

Figure 12. Temporal variation of eccentricity for various K in case of concentric compound drop. The other considered parameters are $\theta_t = \pi/4$, $R_{12} = 1.5$, $R_{13} = 1$, $S_{12} = 2$, $S_{13} = 1$, $\rho_{12} = 1.04$, $\rho_{13} = 1$, $\lambda_{12} = 0.5$, $\lambda_{13} = 1$, $M = 1$, $Ca = 0.1$ and $Re_E = 0.1$.

$$\Omega^1_{n,k}(\xi) = \int_{-1}^{1} \frac{x C_{n+1}^{-1/2} C_{k+1}^{-1/2}}{(1-x^2)}\,\mathrm{d}x, \quad \Omega^2_{n,k}(\xi) = \int_{-1}^{1} \frac{C_{n+1}^{-1/2} C_{k+1}^{-1/2}}{(\cosh\xi - x)}\,\mathrm{d}x, \tag{B6a,b}$$

$$\Omega^3_{n,k}(\xi) = \int_{-1}^{1} \frac{(\cosh\xi - x)^{3/2} C_{n+1}^{-1/2} C_{k+1}^{-1/2}}{(1-x^2)^{3/2}}\,\mathrm{d}x, \quad \Omega^4_{n,k}(\xi) = \int_{-1}^{1} \frac{(\cosh\xi - x)^{1/2} C_{n+1}^{-1/2} C_{k+1}^{-1/2}}{(1-x^2)}\,\mathrm{d}x, \tag{B7a,b}$$

$$\Omega^5_{n,k}(\xi) = \int_{-1}^{1} \frac{x C_{n+1}^{-1/2} C_{k+1}^{-1/2}}{(1-x^2)(\cosh\xi - x)}\,\mathrm{d}x, \quad \Omega^6_{n,k}(\xi) = \int_{-1}^{1} \frac{C_{n+1}^{-1/2} C_{k+1}^{-1/2}}{(\cosh\xi - x)^2}\,\mathrm{d}x, \tag{B8a,b}$$

$$\Omega^7_{n,k}(\xi) = \int_{-1}^{1} \frac{(\cosh\xi - x)^{1/2} C_{n+1}^{-1/2} C_{k+1}^{-1/2}}{(1-x^2)^{3/2}}\,\mathrm{d}x, \quad \Omega^8_{n,k}(\xi) = \int_{-1}^{1} \frac{C_{n+1}^{-1/2} C_{k+1}^{-1/2}}{(\cosh\xi - x)^{1/2}(1-x^2)}\,\mathrm{d}x. \tag{B9a,b}$$

Equations (B1*a*)–(B1*d*) are for $\xi = \xi_1$ and (B1*e*)–(B1*h*) are for $\xi = \xi_2$.

Appendix C. Condition for the validity of the concentric compound drop configuration

In order to determine the condition within which the concentric assumption is valid, we plot the eccentricity variation with time for various K in figure 12. Previously, it has been established that the concentric and eccentric theories deliver similar results when the eccentricity $e < 0.1$ (Mandal *et al.* 2016*b*). From figure 12, we determine that the aforementioned condition is satisfied when the dimensionless time ranges from 450 to 850. Beyond this, the eccentric theory (Jadav & Ghosh 2021*a*,*b*) needs to be applied.

References

Bandopadhyay, A., Mandal, S., Kishore, N.K. & Chakraborty, S. 2016 Uniform electricfield-induced lateral migration of a sedimenting drop. *J. Fluid Mech.* **792**, 553–589.

Basaran, O.A. 2002 Small-scale free surface flows with breakup: drop formation and emerging applications. *AIChE J.* **48** (9), 1842–1848.

Behjatian, A. & Esmaeeli, A. 2013 Electrohydrodynamics of a liquid column under a transverse electric field in confined domains. *Intl J. Multiphase Flow* **48**, 71–81.

https://doi.org/10.1017/jfm.2022.929 Published online by Cambridge University Press

BORUAH, M.P., RANDIVE, P.R., PATI, S. & SAHU, K.C. 2022 Charge convection and interfacial deformation of a compound drop in plane Poiseuille flow under an electric field. *Phys. Rev. Fluid* **7**, 013703.

BRUNN, P.O. & RODEN, T. 1985 On the deformation and drag of a type-A multiple drop at low Reynolds number. *J. Fluid Mech.* **160**, 211–234.

CASTELLANOS, A. 2014 *Electrohydrodynamics*. Springer.

CHOI, S. & SAVELIEV, A.V. 2017 Oscillatory coalescence of droplets in an alternating electric field. *Phys. Rev. Fluids* **2** (6), 063603.

DAS, D. & SAINTILLAN, D. 2016 A nonlinear small-deformation theory for transient droplet electrohydrodynamics. *J. Fluid Mech.* **810**, 225–253.

DEY, R., GHOSH, U.U., CHAKRABORTY, S. & DASGUPTA, S. 2015 Dynamics of electrically modulated colloidal droplet transport. *Langmuir* **31** (41), 11 269–11 278.

DRAXLER, J. & MARR, R. 1986 Emulsion liquid membranes part I: phenomenon and industrial application. *Chem. Engng Process.* **20** (6), 319–329.

EOW, J.S., GHADIRI, M. & SHARIF, A.O. 2007 Electro-hydrodynamic separation of aqueous drops from flowing viscous oil. *J. Petrol. Sci. Engng* **55** (1–2), 146–155.

ESMAEELI, A. & SHARIFI, P. 2011 Transient electrohydrodynamics of a liquid drop. *Phys. Rev.* E **84**, 036308.

FABIILLI, M.L., LEE, J.A., KRIPFGANS, O.D., CARSON, P.L. & FOWLKES, J.B. 2010 Delivery of water-soluble drugs using acoustically triggered perfluorocarbon double emulsions. *Pharmaceut. Res.* **27** (12), 2753–2765.

GAÑÁN-CALVO, A.M., LÓPEZ-HERRERA, J.M., HERRADA, M.A., RAMOS, A. & MONTANERO, J.M. 2018 Review on the physics of electrospray: from electrokinetics to the operating conditions of single and coaxial Taylor cone-jets, and AC electrospray. *J. Aerosol Sci.* **125**, 32–56.

GOUZ, H.N. & SADHAL, S.S. 1989 Fluid dynamics and stability analysis of a compound droplet in an electric field. *Q. J. Mech. Appl. Maths* **42** (1), 65–83.

HA, J.-W. & YANG, S.-M. 2000 Rheological responses of oil-in-oil emulsions in an electric field. *J. Rheol.* **44** (2), 235–256.

HAPPEL, J. & BRENNER, H. 2012 Low Reynolds number hydrodynamics: with special applications to particulate media. Springer.

JADHAV, S.N. & GHOSH, U. 2021*a* Thermocapillary effects on eccentric compound drops in Poiseuille flows. *Phys. Rev. Fluid* **6**, 073602.

JADHAV, S.N. & GHOSH, U. 2021*b* Effect of surfactant on the settling of a drop towards a wall. *J. Fluid Mech.* **912**, A4.

JAWOREK, A. & KRUPA, A. 1999 Jet and drops formation in electrohydrodynamic spraying of liquids: a systematic approach. *Exp. Fluids* **27** (1), 43–52.

JOHNSON, R.E. & SADHAL, S.S. 1985 Fluid mechanics of compound multiphase drops and bubbles. *Annu. Rev. Fluid Mech.* **17** (1), 289–320.

KARYAPPA, R.B., DESHMUKH, S.D. & THAOKAR, R.M. 2014 Breakup of a conducting drop in a uniform electric field. *J. Fluid Mech.* **754**, 550–589.

KARYAPPA, R.B., NAIK, A.V. & THAOKAR, R.M. 2016 Electroemulsification in a uniform electric field. *Langmuir* **32** (1), 46–54.

KIM, S.-H., KIM, J.W., CHO, J.-C. & WEITZ, D.A. 2011 Double-emulsion drops with ultra-thin shells for capsule templates. *Lab Chip* **11**, 3162.

LAC, E. & HOMSY, G.M. 2007 Axisymmetric deformation and stability of a viscous drop in a steady electric field. *J. Fluid Mech.* **590**, 239–264.

MANDAL, S., BANDOPADHYAY, A. & CHAKRABORTY, S. 2016*a* The effect of uniform electric field on the cross-stream migration of a drop in plane Poiseuille flow. *J. Fluid Mech.* **809**, 726–774.

MANDAL, S., GHOSH, U. & CHAKRABORTY, S. 2016*b* Effect of surfactant on motion and deformation of compound droplets in arbitrary unbounded Stokes flows. *J. Fluid Mech.* **803**, 200–249.

MANDAL, S., SINHA, S., BANDOPADHYAY, A. & CHAKRABORTY, S. 2018 Drop deformation and emulsion rheology under the combined influence of uniform electric field and linear flow. *J. Fluid Mech.* **841**, 408–433.

MORTON, D.S., SUBRAMANIAN, R.S. & BALASUBRAMANIAM, R. 1990 The migration of a compound drop due to thermocapillarity. *Phys. Fluids* A **2** (12), 2119.

NAKANO, M. 2000 Places of emulsions in drug delivery. *Adv. Drug Deliv. Rev.* **45** (1), 1–4.

PAK, O.S., FENG, J. & STONE, H.A. 2014 Viscous Marangoni migration of a drop in a Poiseuille flow at low surface Péclet numbers. *J. Fluid Mech.* **753**, 535–552.

PALANIAPPAN, D. & DARIPA, P. 2000 Compound droplet in extensional and paraboloidal flows. *Phys. Fluids* **12** (10), 2377.

https://doi.org/10.1017/jfm.2022.929 Published online by Cambridge University Press

PETHIG, R. 2013 Dielectrophoresis: an assessment of its potential to aid the research and practice of drug discovery and delivery. *Adv. Drug Deliv. Rev.* **65** (11–12), 1589–1599.

PODDAR, A., MANDAL, S., BANDOPADHYAY, A. & CHAKRABORTY, S. 2018 Sedimentation of a surfactant-laden drop under the influence of an electric field. *J. Fluid Mech.* **849**, 277–311.

PODDAR, A., MANDAL, S., BANDOPADHYAY, A. & CHAKRABORTY, S. 2019 Electrical switching of a surfactant coated drop in Poiseuille flow. *J. Fluid Mech.* **870**, 27–66.

RUSHTON, E. & DAVIES, G.A. 1983 Settling of encapsulated droplets at low Reynolds numbers. *Intl J. Multiphase Flow* **9** (3), 337–342.

SADHAL, S.S. 1983 A note on the thermocapillary migration of a bubble normal to a plane surface. *J. Colloid Interface Sci.* **95**, 283–285.

SADHAL, S.S. & OGUZ, H.N. 1985 Stokes flow past compound multiphase drops: the case of completely engulfed drops/bubbles. *J. Fluid Mech.* **160**, 511–529.

SANTRA, S., DAS, S. & CHAKRABORTY, S. 2020 Electrically modulated dynamics of a compound droplet in a confined microfluidic environment. *J. Fluid Mech.* **882**.

SANTRA, S., MANDAL, S. & CHAKRABORTY, S. 2019 Confinement effect on electrically induced dynamics of a droplet in shear flow. *Phys. Rev.* E **100** (3), 33101.

SONI, P., DIXIT, D. & JUVEKAR, V.A. 2017 Effect of conducting core on the dynamics of a compound drop in an AC electric field. *Phys. Fluids* **29** (11), 112108.

SONI, P., JUVEKAR, V.A. & NAIK, V.M. 2013 Investigation on dynamics of double emulsion droplet in a uniform electric field. *J. Electrostat.* **71** (3), 471–477.

SONI, P., THAOKAR, R.M. & JUVEKAR, V.A. 2018 Electrohydrodynamics of a concentric compound drop in an AC electric field. *Phys. Fluids* **30** (3), 032102.

STIMSON, M. & JEFFERY, G.B. 1926 The motion of two spheres in a viscous fluid. *Proc. R. Soc. Lond.* A **111** (757), 110–116.

STONE, H.A. & LEAL, L.G. 1990 Breakup of concentric double emulsion droplets in linear flows. *J. Fluid Mech.* **211**, 123–156.

TAYLOR, G. 1966 Studies in electrohydrodynamics. I. The circulation produced in a drop by electrical field. *Proc. R. Soc. Lond.* A **291** (1425), 159–166.

TSUKADA, T., MAYAMA, J., SATO, M. & HOZAWA, M. 1997 Theoretical and experimental studies on the behavior of a compound drop under a uniform DC electric field. *J. Chem. Engng Japan* **30** (2), 215–222.

UTADA, A.S., LORENCEAU, E., LINK, D.R., KAPLAN, P.D., STONE, H.A. & WEITZ, D.A. 2005 Monodisperse double emulsions generated from a microcapillary device. *Science* **308** (5721), 537–541.

VLAHOVSKA, P.M. 2011 On the rheology of a dilute emulsion in a uniform electric field. *J. Fluid Mech.* **670**, 481–503.

WACHOLDER, E. & WEIHS, D. 1972 Slow motion of a fluid sphere in the vicinity of another sphere or a plane boundary. *Chem. Engng Sci.* **27** (10), 1817–1828.

WARD, T. & HOMSY, G.M. 2006 Chaotic streamlines in a translating drop with a uniform electric field. *J. Fluid Mech.* **547**, 215–230.

XU, X. & HOMSY, G.M. 2006 The settling velocity and shape distortion of drops in a uniform electric field. *J. Fluid Mech.* **564**, 395–414.

YARIV, E. & ALMOG, Y. 2016 The effect of surface-charge convection on the settling velocity of spherical drops in a uniform electric field. *J. Fluid Mech.* **797**, 536–548.

ZHANG, J., ZAHN, J. & LIN, H. 2013 Transient solution for droplet deformation under electric fields. *Phys. Rev.* E **87** (4), 043008.

ZHENG, B., TICE, J.D. & ISMAGILOV, R.F. 2004 Formation of droplets of alternating composition in microfluidic channels and applications to indexing of concentrations in droplet-based assays. *Anal. Chem.* **76** (17), 4977–4982.

https://doi.org/10.1017/jfm.2022.929 Published online by Cambridge University Press